J. Fluid Mech. (2011), *vol.* 672, *pp.* 5–32.
doi:10.1017/S0022112010006087

Stabilizing effect of surrounding gas flow on a plane liquid sheet

OUTI TAMMISOLA[1], ATSUSHI SASAKI[2], FREDRIK LUNDELL[1,3]†, MASAHARU MATSUBARA[2] AND L. DANIEL SÖDERBERG[3,4]

[1]Linné Flow Centre, KTH Mechanics, Royal Institute of Technology, SE-100 44 Stockholm, Sweden

[2]Mechanical Systems Engineering, Shinshu University, Nagano 380-8553, Japan

[3]Wallenberg Wood Science Center, KTH Mechanics, Royal Institute of Technology, SE-100 44 Stockholm, Sweden

[4]Innventia AB, Box 5604, SE-114 86 Stockholm, Sweden

(Received 2 May 2010; revised 30 August 2010; accepted 17 November 2010; first published online 18 February 2011)

The stability of a plane liquid sheet is studied experimentally and theoretically, with an emphasis on the effect of the surrounding gas. Co-blowing with a gas velocity of the same order of magnitude as the liquid velocity is studied, in order to quantify its effect on the stability of the sheet. Experimental results are obtained for a water sheet in air at Reynolds number $Re_l = 3000$ and Weber number $We = 300$, based on the half-thickness of the sheet at the inlet, water mean velocity at the inlet, the surface tension between water and air and water density and viscosity. The sheet is excited with different frequencies at the inlet and the growth of the waves in the streamwise direction is measured. The growth rate curves of the disturbances for all air flow velocities under study are found to be within 20 % of the values obtained from a local spatial stability analysis, where water and air viscosities are taken into account, while previous results from literature assuming inviscid air overpredict the most unstable wavelength with a factor 3 and the growth rate with a factor 2. The effect of the air flow on the stability of the sheet is scrutinized numerically and it is concluded that the predicted disturbance growth scales with (i) the absolute velocity difference between water and air (inviscid effect) and (ii) the square root of the shear from air on the water surface (viscous effect).

Key words: instability control, interfacial flows (free surface), jets

1. Introduction

Instability or breakup of a round or flat liquid jet entering into a gas or vacuum is important in a vast number of applications (Eggers & Villermaux 2008 and references therein). In many cases, such as combustion, agriculture and chemical or process engineering, it is desirable that the jet breaks up and forms a spray. The reason is naturally that one wants to achieve mixing between the gas and the liquid or an efficient spreading of the liquid. We however aim at *stabilizing* a liquid jet. An application where stabilization is desirable is papermaking, where a plane jet of pulp

† Email address for correspondence: fredrik@mech.kth.se

suspension (a suspension of mainly water and cellulose fibres) is sprayed onto one or in between two permeable wires. As the water is drained, the fibres remain on the wire(s) and form the paper.

The stability of liquid jets surrounded by gas is a classical problem in fluid mechanics. The stability of round liquid jets was studied by Rayleigh (1878), who in an inviscid study concluded that all long enough round jets break down into droplets due to surface tension. The physical reason is that small waves result in an axial variation of the radius and therefore a capillary pressure gradient that makes the fluid to migrate even more to the thinner sections. Later on, Weber (1931) studied the effect of a velocity difference between liquid and gas and concluded that this should increase the instability. Plane jets, or liquid sheets, are different from round jets, since far from the rims, there is no surface force binding the upper and lower surfaces together; the equilibrium is reached when both surfaces are flat and parallel. Squire (1953) showed that liquid sheets do not possess the kind of instability caused by surface tension alone that Rayleigh (1878) found for round jets.

In order to explain instabilities of liquid sheets, it is thus necessary to add more physics to the analysis. Hagerty & Shea (1955) introduced an inviscid stationary gas around the sheet and Li & Tankin (1991) and Li (1993) added the viscosity of the liquid. Further on, Teng, Lin & Chen (1997) performed a linear stability analysis of a specific wall-bounded configuration including viscosity and velocity profiles of the surrounding air as well, and Söderberg & Alfredsson (1998) did the same for a free liquid sheet. The latter analysis is the basis for the theoretical part of the present work. Recently, Sander & Weigand (2008) performed a direct numerical simulation on the wave growth and breakup of a liquid jet and investigated the effects of the physical parameters, as well as initial velocity profile and turbulence intensity, on the breakup process. A very brief summary of the studies above is: (i) the instability of liquid sheets is driven by a velocity difference between liquid and gas, (ii) symmetric and antisymmetric modes can exist depending on the parameter regime, (iii) liquid viscosity has a stabilizing effect in most cases and (iv) the inlet profile has a remarkable effect on the instability.

In experiments, liquid sheets have mainly been studied through flow visualizations and measurements of integral quantities such as breakup length and spray angle. Söderberg & Alfredsson (1998) studied a liquid sheet forced by a loudspeaker, and the disturbances showed qualitative agreement with the linear stability theory. The particular case of a liquid sheet with a co-flowing gas, which is studied in the present work, has been investigated by Mansour & Chigier (1991), Lozano *et al.* (2001) and Park *et al.* (2004). In these studies, a strong blowing was applied in order to imitate the atomization process.

In the present work, a liquid sheet surrounded by gas, with and without co-flow, is generated experimentally and disturbed in a controlled manner. The growth of disturbances on the sheet is carefully quantified by measuring the variation in time of the local surface inclination. As a result, growth factors can be determined with good accuracy. The results are compared with theoretical predictions based on the method by Söderberg & Alfredsson (1998), which has been complemented to account for co-flowing air. The experimental set-up and measurement techniques are presented in § 2 and the theoretical and numerical methods are explained in § 3. In § 4, the experimental results are presented and compared with the theoretical predictions. Additional observations based on the theory are made in § 5 and, finally, the conclusions are drawn in § 6.

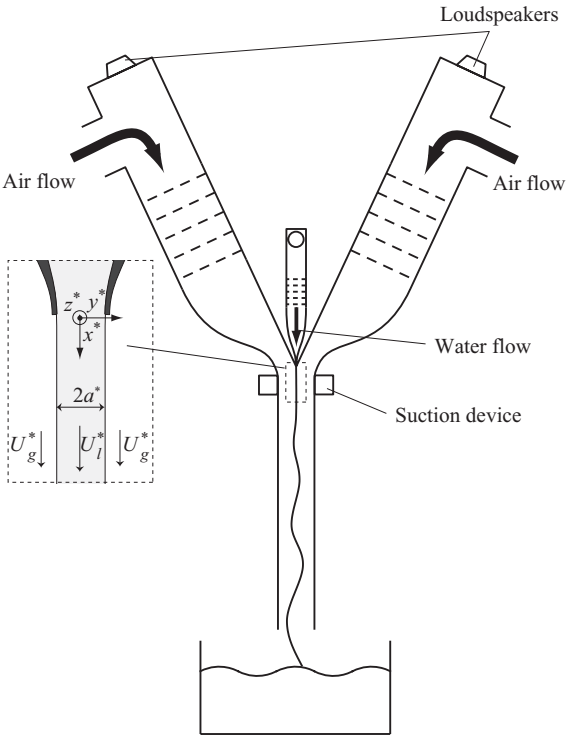

FIGURE 1. Schematic of the experimental set-up: nozzles, sheet, basin and coordinate system.

2. Experimental set-up and methods

2.1. *Liquid sheet facility*

The experiments were performed in a liquid sheet facility at Shinshu University, Nagano, Japan. The facility consists of a nozzle unit (see figure 1) ejecting a water sheet vertically into a water basin. The coordinate system is defined in the figure, and is x^*, y^*, z^* for the streamwise, sheet-normal and spanwise directions, respectively, where asterisks denote dimensional quantities. The origin is located at the centre of the exit of the water nozzle. Furthermore, the sheet half-thickness is denoted by a^*, the velocity profile in the liquid by U_l^* and the velocity profile in the gas by U_g^*, while U_l^{0*} is the surface velocity of the liquid and $U_g^{\infty *}$ the free-stream velocity of the gas.

The nozzle unit consists of three parts: one central nozzle for the water and two side nozzles for the co-flowing air. All of them have contractions near the outlet in order to generate as flat velocity profiles as possible. The width of the exits in the z^*-direction is 400 mm and the thickness in the y^*-direction is 1 mm for the water nozzle and 50 mm for each air nozzle. Because of design constraints, the air streams have an angle of 25° to the water sheet at the outlet, as indicated in figure 1.

The water is pumped in a closed loop by a centrifugal pump and the air is taken from the room and pressurized with a fan before entering the nozzles via dampers and flow regulators. The nominal velocities of air and water are the mean velocities over the cross-sections. The sheet can be forced to oscillate at a given frequency by speakers mounted at the counter-ends of the flow regulators.

Inclination of the air flow nozzles relative to the water sheet is a necessary design constraint, to get a sufficient contraction for the sheet prior to the nozzle. To avoid

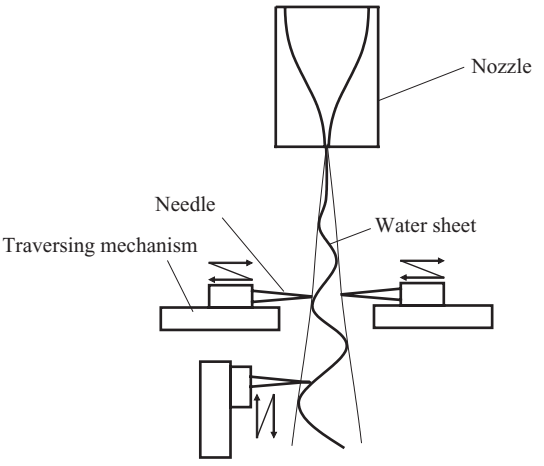

FIGURE 2. Measurement system for the thickness of the liquid sheet.

inclination of the air free-stream velocity, suction is applied at the walls near the outlet. Furthermore, the air flow is surrounded by walls of length 500 mm at a sheet-normal distance of 50 mm from the centreline, to create a constant and parallel air free-stream velocity.

2.2. *Experimental methods*

The flow rates are monitored and adjusted by checking the pressure drops over the nozzles during all experiments. In order to verify the flow quality, velocity and thickness measurements are performed. The velocity is measured by traversing a hot wire (air) and a total pressure tube (water) in the y^*-direction. These sensors allow the spatial variations of the mean flow to be quantified.

The thickness of the liquid sheet is measured by the system sketched in figure 2, by moving 10 pairs of sharp electrodes towards the surface of the liquid sheet from both sides with an accurate traversing mechanism. First, a reference position is determined by moving the electrodes towards a 1 mm thick gauge inserted between them until the circuit is closed. After turning on the water flow, the position of each side of the liquid sheet can be determined by moving the relevant electrode out from the liquid sheet and then traverse it towards the sheet again until it touches the surface and the circuit is closed again.

Finally, the amplitude of the sheet oscillations is measured. This is done with a laser and a photodiode array as shown in figure 3. A horizontal laser sheet is focused on the water surface by a cylindrical lens so that the measurement area is point-like. From there the light is again scattered in the spanwise direction, and the angle of reflection in the vertical direction is given by the local streamwise inclination angle of the water surface. The reflection from the measurement point thus forms a light sheet that is detected with the photodiode array. This in-house-made optical system allows a continuous measurement of the inclination angle of the water surface θ, while waves pass by the measurement point.

By detecting θ over time we get time sequences as shown in figure 4. The phase velocity estimated from these example signals is $7.42\,\mathrm{m\,s^{-1}}$, corresponding to the mean water speed $7.3\,\mathrm{m\,s^{-1}}$. The feature that the phase velocity is almost equal to the sheet velocity is observed for a wide range of frequencies from 40 to 200 Hz. The reason for the slight deviation between the phase velocity and the mean water speed ($<2\,\%$) is

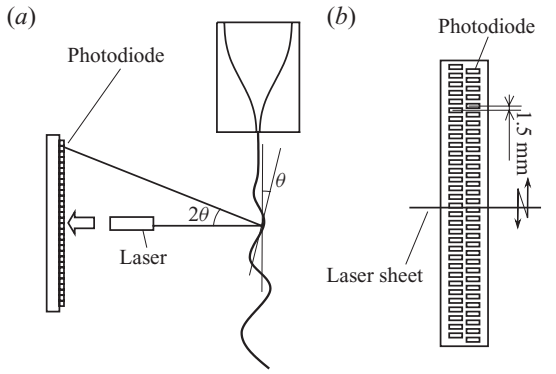

FIGURE 3. Measurement system for the local angle of the sheet surface: (*a*) liquid sheet and laser beam and (*b*) photodiode array.

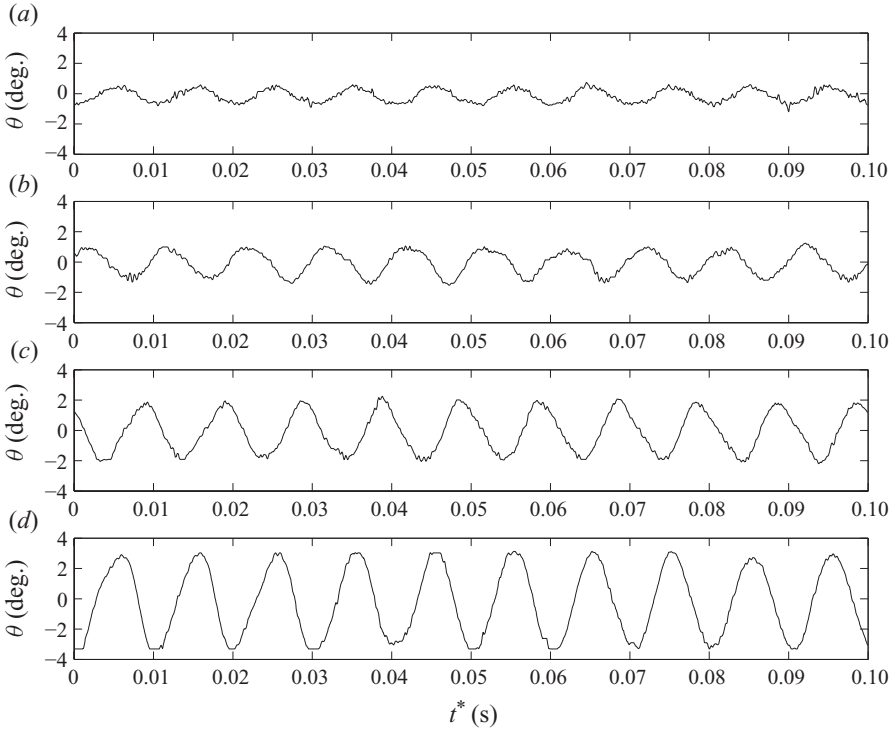

FIGURE 4. Time signals of the surface angle for a water sheet experiment. The initial disturbance frequency is 100 Hz. Measurement location: (*a*) $x^* = 250$ mm (non-dimensional, $x \approx 500$); (*b*) $x^* = 300$ mm (non-dimensional, $x \approx 600$); (*c*) $x^* = 350$ mm (non-dimensional, $x \approx 700$) and (*d*) $x^* = 400$ mm (non-dimensional, $x \approx 800$).

probably that the determination of the mean water speed is somewhat less accurate than the measurement of the phase velocity.

From the time signals, the local oscillation amplitude and phase can be evaluated. The growth rate is then obtained from the slope of the amplitude curve in a logarithmic diagram.

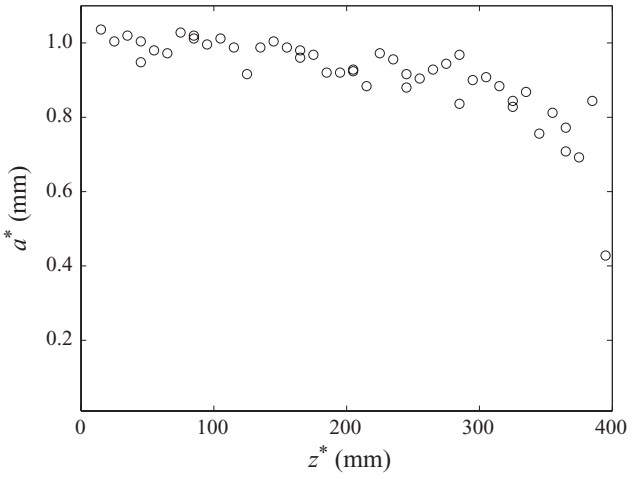

FIGURE 5. Thickness variation of the liquid sheet in the spanwise direction.

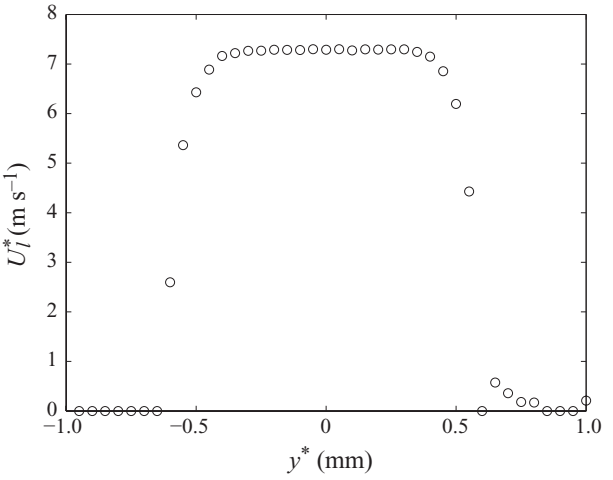

FIGURE 6. Streamwise velocity as a function of y^* just after the nozzle exit.

2.3. *Flow characteristics*

The flow quality in the apparatus is quantified in figures 5–7. The results on the liquid sheet are given without gas flow, whereas the gas flow results are taken without water – the reason for this is detailed below.

The thickness of the sheet as a function of the spanwise position is shown in figure 5. It varies from around 800 μm on one side to 1000 μm on the other. This variation, $\pm 10\,\%$, is indeed substantial. Nevertheless, the flow visualizations to be shown in § 4.1 reveal that the disturbances on the sheet are very two-dimensional.

The contraction of the water nozzle prior to the outlet aims at creating a top-hat velocity profile and the water velocity data in figure 6 show that it succeeds fairly well. The shear layers at the sides are thin and the plateau is flat. Here, it has to be mentioned that towards the rims at $y^* = \pm 0.5$ mm, small fluctuations of the position of the sheet give rise to a decrease in the mean velocity measured by the total pressure tube. This decrease occurs because the tube is intermittently exposed to air and water, respectively. Consequently, the velocity profile in figure 6 overestimates

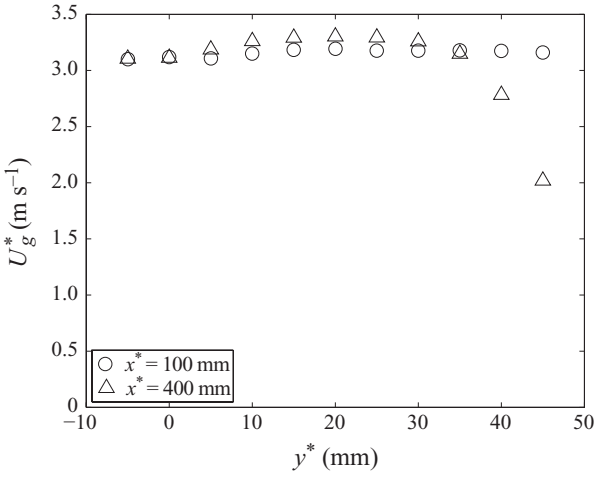

FIGURE 7. Distribution of the streamwise velocity in the air flow at two different distances from the nozzle.

the actual shear layers of the liquid sheet. The gravitational acceleration for the sheet in the measurement region was seen to be of the order of 1 %.

The velocity profile of the air as a function of y^* at two different streamwise positions is shown in figure 7. Since a hot wire is used, the measurements are taken without water flow. There are two main reasons for this. The first is that the wire might break if hit by drops, and the second reason is that the heat transfer from the wire to the air, which is used to determine the air velocity U_g^*, changes with the air humidity. Thus, in order to get accurate data of the air velocity, the sheet cannot be present.

Figure 7 shows that the air velocity is constant and fairly parallel to the sheet in the region $y^* = -5$ mm to $y^* = 5$ mm (remember the sheet thickness 1.1 mm). The deviation in the free-stream velocity is of the order of 3 % in this region. Further out from the sheet, there is a difference of 0.1 m s^{-1} between the two streamwise stations.

The observed shear in the air free stream will be of secondary importance, since the deviation between water and air velocities will always be an order of magnitude larger in all cases that are studied in detail. Near the walls surrounding the air flow, located at $y^* = \pm 50$ mm, there is a clear boundary-layer development and therefore a velocity decrease at $x^* = 400$ mm. However, this boundary layer is far enough from the sheet so that the free-stream velocity near the sheet remains unaffected in the measurement region.

3. Theoretical and numerical methods

The velocities are non-dimensionalized with U_l^{0*} and the lengths with a^*, again all dimensional quantities marked with asterisks. In the following, we denote the non-dimensional liquid velocity profile by $U_l(y)$, the gas velocity profile by $U_g(y)$ and the free-stream velocity of the gas (normalized by liquid velocity) by U_g^∞. Recall from figure 1 that x is the streamwise, y is the sheet-normal and z is the spanwise direction.

In this way, the problem is characterized by the following four non-dimensional parameters.

Firstly, we have the overall Reynolds number

$$Re_l = \frac{U_l^{0*} a^*}{\nu_l^*} \tag{3.1}$$

and the Weber number

$$We = \frac{\rho_l^* \left(U_l^{0*}\right)^2 a^*}{\gamma^*}, \tag{3.2}$$

where ν_l^* is the kinematic viscosity of the liquid, ρ_l^* is its density and γ^* is the surface tension between the liquid and the gas. Here We describes the ratio between inertia and capillary forces, and will enter the problem through the interface boundary conditions as will be explained in § 3.2. We also need the density ratio between the gas and the liquid,

$$\tilde{\rho} = \frac{\rho_g^*}{\rho_l^*} \tag{3.3}$$

and, similarly, the viscosity ratio

$$\tilde{\mu} = \frac{\mu_g^*}{\mu_l^*}. \tag{3.4}$$

In two-dimensional linear stability, all flow variables are divided into a steady base flow (capital letters) and a disturbance (small letters) as follows:

$$\boldsymbol{U}_{tot}(x, y, z, t) = \boldsymbol{U}(x, y) + \boldsymbol{u}(x, y, z, t), \tag{3.5}$$

$$P_{tot}(x, y, z, t) = P(x, y) + p(x, y, z, t). \tag{3.6}$$

In the following subsections, we will explain how both of them are obtained.

3.1. *Determination of the base flow*

The base flow in the liquid is assumed to be uniform, based on the experimental profiles – the deviation from uniform velocity was estimated to be less than 1 %, and the shape of the liquid velocity profile was hard to calculate numerically with that accuracy.

Since it was not possible to measure the air boundary layer in the presence of the liquid sheet, it has to be modelled. We present results for two alternative models in this paper, denoted as Sakiadis and Stokes boundary layers. The first one is formally a solution to the boundary-layer equations, whereas the second one is not, but admits a convenient analytical solution.

3.1.1. *Model I: modified Sakiadis boundary layer*

This profile is obtained from the similarity solution for the boundary-layer equations in a manner analogous to the Blasius boundary layer over a flat plate. We introduce a non-dimensional streamfunction f such that

$$f'(\eta) = U_g(y), \quad \eta = (y - 1)\sqrt{\frac{Re_g}{x}}, \tag{3.7}$$

where

$$Re_g = \frac{\tilde{\rho} Re_l}{\tilde{\mu}}. \tag{3.8}$$

The boundary-layer equation and the boundary conditions ($U_g = 1$ on the sheet surface and $U = U_g^\infty$ far away from the sheet) then read

$$ff'' + 2f''' = 0, \tag{3.9}$$

$$f'(1) = 1 \tag{3.10}$$

and

$$f'(\infty) = U_g^\infty. \tag{3.11}$$

This equation coupled with the boundary condition $U_g^\infty = 0$ was first studied by Sakiadis (1961*a*), and is therefore termed Sakiadis boundary layer in this paper.

3.1.2. *Model II: modified Stokes layer*

This model was used in Söderberg (2003) and is based on the Stokes first problem, the flow above an instantaneously started plate. The solution to this problem is analytical, and therefore especially easy to include also in problems with a varying liquid velocity profile in the streamwise direction, as in Söderberg (2003). In this case, the air velocity is obtained as

$$U_g^* = U_l^{0*} + \left(U_g^{\infty *} - U_l^{0*}\right) \mathrm{erf}(\eta^*/2), \tag{3.12}$$

where erf is the error function, and

$$\eta^* = (y^* - a^*)/\sqrt{\nu_g^* t^*}, \tag{3.13}$$

where ν_g^* is the kinematic viscosity of the gas. To be able to use this solution, we must define t^* as a function of x^* in such a way that gives a qualitatively correct growth of the gas boundary layer in the streamwise direction. The choice here is

$$t^* = \frac{U_l^{0*}}{x^*}. \tag{3.14}$$

The resulting equation is in non-dimensional form

$$U_g = 1 + \left(U_g^\infty - 1\right) \mathrm{erf}(\eta/2), \tag{3.15}$$

where, as before,

$$\eta = (y - 1)\sqrt{\frac{Re_g}{x}}. \tag{3.16}$$

3.1.3. *Parametrization of the base flow profiles*

As mentioned, the liquid base flow profile was assumed to be uniform. The experimental velocity profile of the water just after the nozzle exit is shown in figure 6. The boundary layers are thin enough that this profile should have relaxed to a uniform one at all measurement positions, located at least 300 jet thicknesses downstream from the nozzle.

The uniformity also means that the non-dimensional parameters Re_l and We for the liquid sheet are constant in the streamwise direction. While Re is indeed constant

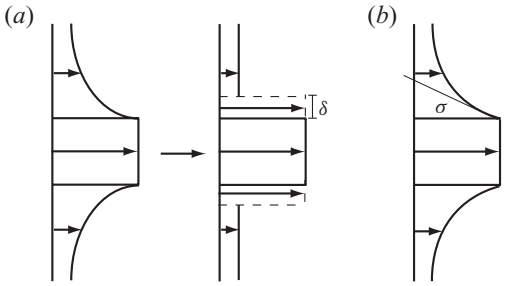

FIGURE 8. (*a*) Physical interpretation of the boundary-layer thickness δ (3.17). (*b*) Illustration of σ.

due to mass conservation, the small gravitational acceleration of the sheet in the measurement region (§ 2.3) results in an increase of We of the order of 1 %. This variation is of the same order as the uncertainty due to e.g. temperature fluctuations, and was therefore not considered.

The streamwise development of the whole flow can thus be characterized by one additional parameter, e.g. the boundary-layer thickness δ that we define by

$$\delta = \int_1^\infty \frac{\left(U_g(y) - U_g^\infty\right)}{\left(1 - U_g^\infty\right)} \mathrm{d}y. \tag{3.17}$$

This δ is similar to the displacement thickness for a boundary layer around a solid body in the way that it gives the height by which the liquid sheet should be extended in the sheet-normal direction to get the same total volume flow, if both liquid and gas flows were considered inviscid. In a real inviscid calculation, it might be desirable to keep the total mass flow constant instead of volume flow, in which case the height of the extensional region is effected by the density ratio. However, we prefer to define the boundary-layer thickness based on the gas properties.

The same definition of δ was also used by Sakiadis (1961*b*) in the stagnant air case, and termed displacement thickness in that paper. However, we would like to point out that it does not have a physical interpretation in terms of displacement of streamlines like for the Blasius boundary layer, but rather represents a displacement of the free-stream region.

Another alternative to characterize the flow that will be considered is the shear on the liquid surface, σ. Both parameters are illustrated in figure 8. The Sakiadis solution has a larger δ and a larger absolute value of σ than Stokes at the same streamwise position, as detailed in figure 9.

When the air velocity U_g^∞ is added as a parameter, the shape of the Stokes profile only depends on the absolute velocity difference between water and air, while the Sakiadis profiles are different for $U_g^\infty < 1$ and $U_g^\infty > 1$ (figure 10). This difference is also reflected in δ and σ (figure 11). The resulting full base flow field $U(x, y)$ for $U_g^\infty = 0$ and the Stokes model is shown with grey-scale in figure 12.

3.2. *Linear stability analysis*

In the linear stability analysis, two separate sets of equations are solved – one for the liquid and the other for the gas phase, with $Re = Re_l$ and $Re = Re_g$, respectively. Both

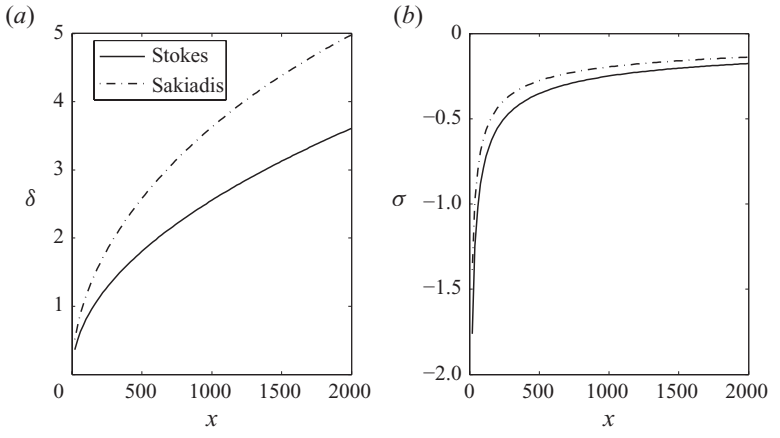

FIGURE 9. (*a*) The boundary-layer thickness δ as a function of the streamwise distance x for the Stokes (—) and Sakiadis (- -) base flow models, $U_g^\infty = 0$. (*b*) Plot of σ, the shear from air at the surface, as a function of x, Stokes (—) and Sakiadis (- -), $U_g^\infty = 0$.

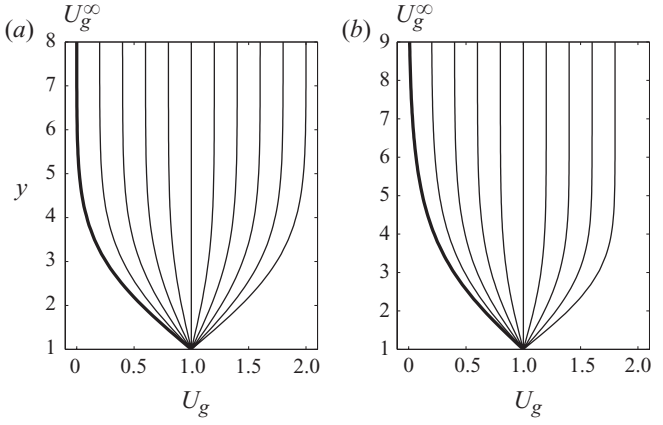

FIGURE 10. The base flow profiles with different amount of 'blowing' for (*a*) the Stokes model (*b*) the Sakiadis model. The profile for $U_g^\infty = 0$ is drawn with a thick line, and thereafter $U_g^\infty = 0.2, 0.4, \ldots, 2$. For the Stokes model in (*a*), the profiles are exactly symmetric with respect to the difference between the liquid and gas velocities, while for the Sakiadis model in (*b*) they are not.

share the same form as presented below. These equations are then coupled together by the interface conditions presented in § 3.2.1.

The Navier–Stokes equations, linearized around a two-dimensional base flow $(\boldsymbol{U}(x, y), P(x, y))$ and with pure base flow terms subtracted, become

$$-\frac{\partial u}{\partial t} - U\frac{\partial u}{\partial x} - V\frac{\partial u}{\partial y} - u\frac{\partial U}{\partial x} - v\frac{\partial U}{\partial y} - \frac{\partial p}{\partial x} + \frac{1}{Re}\left(\frac{\partial^2 u}{\partial^2 x} + \frac{\partial^2 u}{\partial^2 y} + \frac{\partial^2 u}{\partial^2 z}\right) = 0, \quad (3.18)$$

$$-\frac{\partial v}{\partial t} - U\frac{\partial v}{\partial x} - V\frac{\partial v}{\partial y} - u\frac{\partial V}{\partial x} - v\frac{\partial V}{\partial y} - \frac{\partial p}{\partial y} + \frac{1}{Re}\left(\frac{\partial^2 v}{\partial^2 x} + \frac{\partial^2 v}{\partial^2 y} + \frac{\partial^2 v}{\partial^2 z}\right) = 0, \quad (3.19)$$

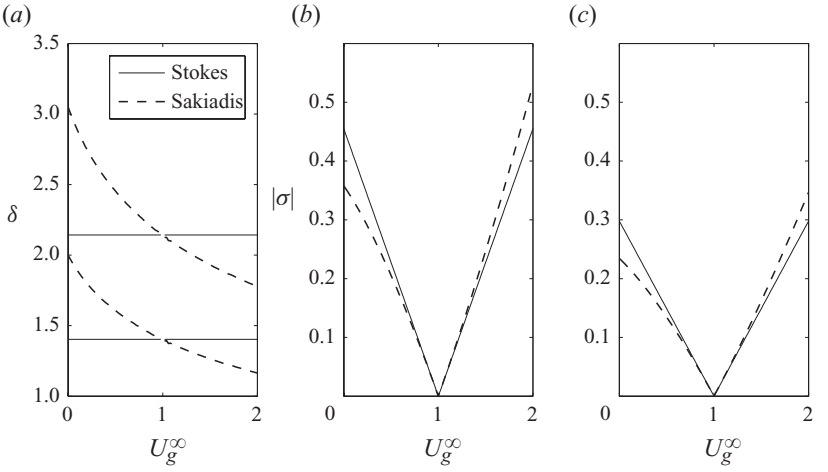

FIGURE 11. (*a*) The boundary-layer thickness δ as a function of the blowing velocity U_g^∞ for the Stokes (—) and Sakiadis (- -) base flow models for two different x-positions, $x = 300$ (lower) and $x = 700$ (upper). The absolute value of the shear from air at the surface as a function of U_g^∞, Stokes (—) and Sakiadis (- -): (*b*) $x = 300$ and (*c*) $x = 700$.

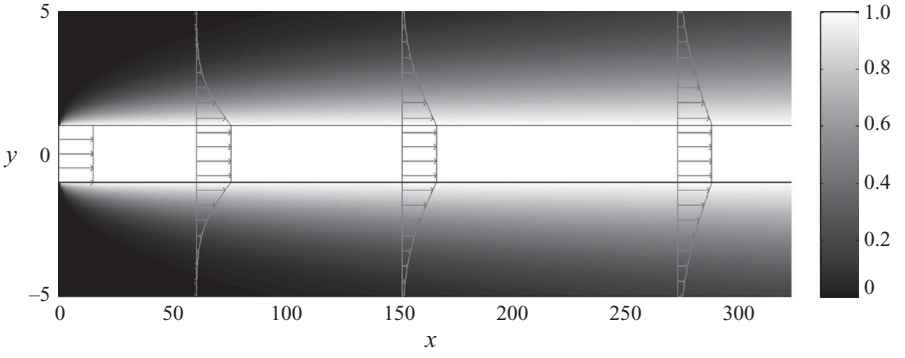

FIGURE 12. The streamwise velocity of the base flow with the Stokes gas flow model in grey-scale, values are indicated by the colour bar. The velocity profiles at $x = 0$, $x = 60$, $x = 150$ and $x = 270$ are plotted with grey arrows on top of the picture. The boundary between the liquid and gas phases is marked by a dark solid line. The liquid velocity profile is uniform all way through, and the streamwise development of the gas boundary layer is seen.

$$-\frac{\partial w}{\partial t} - U\frac{\partial w}{\partial x} - V\frac{\partial w}{\partial y} - \frac{\partial p}{\partial z} + \frac{1}{Re}\left(\frac{\partial^2 w}{\partial^2 x} + \frac{\partial^2 w}{\partial^2 y} + \frac{\partial^2 w}{\partial^2 z}\right) = 0, \tag{3.20}$$

$$\frac{\partial u}{\partial x} + \frac{\partial v}{\partial y} + \frac{\partial w}{\partial z} = 0. \tag{3.21}$$

The stability analysis is based on the assumption that the base flow variations occur on a much longer length scale than the typical wavelength of the disturbances, i.e. *locally parallel flow*. The choice of a local method is supported by the fact that in the experiments the growth rate changes very slowly in the streamwise direction. Both the sheet-normal velocity and all streamwise derivatives of the base flow are neglected,

considering only base flow velocity profiles of the type

$$\boldsymbol{U} = (U(y), 0, 0). \tag{3.22}$$

This results in that all coefficients in front of the disturbance quantities in equations (3.18)–(3.21) are independent of both x and t. Thus, we can Fourier-transform in x and t, making the well-known local Ansatz:

$$\boldsymbol{u}(x, y, t) = (\hat{u}(y), \hat{v}(y))\, \mathrm{e}^{\mathrm{i}(\alpha x - \omega t)}, \tag{3.23}$$

and similarly for p, where α is the wavenumber in the streamwise direction. The spanwise wavenumber is set to zero, as well as the spanwise velocity component, which is justified by the two-dimensional nature of the disturbances in the present experiment.

This is further converted to the velocity–vorticity formulation, which gives the well-known Orr–Sommerfeld equation for the sheet-normal disturbance velocity v (for a derivation, see Schmid & Henningson 2001) for gas and liquid:

$$(\mathrm{i}\alpha U - \mathrm{i}\omega)(D^2 - \alpha^2)\hat{v}_{l,g} - \mathrm{i}\alpha D^2 U \hat{v}_{l,g} = Re_{l,g}^{-1}(D^4 - 2\alpha^2 D^2 + \alpha^4), \tag{3.24}$$

where $D = \mathrm{d}/\mathrm{d}y$ and $Re_{l,g}$ is the Reynolds number in liquid or gas (given by (3.1) and (3.8), respectively). The two sets of equations are coupled by the interface boundary conditions that will be presented in § 3.2.1. We select the centreline of the sheet ($y = 0$) to be the lower boundary of the computational domain and set an antisymmetry condition there, and a no-slip condition at the upper boundary located in the gas free stream. The upper boundary is chosen to be sufficiently far away from the sheet in order to make the results independent of this boundary condition.

The local spatial growth rates for the base flows represented in § 3.1 are calculated numerically with a Chebyshev-discretization in the sheet-normal direction. In spatial analysis, the frequency ω is assumed real while the spatial growth rate and wavenumber are sought. This is similar to the experiments, where the sheet is forced at a given temporal frequency and the spatial growth rate is measured. With this approach, the equations constitute a generalized polynomial eigenvalue problem with the complex eigenvalue $\alpha = \alpha_r + \mathrm{i}\alpha_i$, where the real part α_r gives the wavenumber of a disturbance, while the growth rate $-\alpha_i$ is given by the imaginary part. The disturbance shape corresponding to each eigenvalue comes from the complex eigenfunctions $\hat{v}_{l,g}$.

This fourth-order polynomial generalized eigenvalue problem is converted to a first-order one by a straightforward procedure suggested by Schmid & Henningson (2001). The problem can then be solved by standard methods for eigenvalue calculations. In this work, the EISPACK Fortran Package was used, since it had been used previously for this code (in Söderberg 2003 and Söderberg & Alfredsson 1998), and also because of good numerical stability properties compared with some other solvers for this particular problem. The solver is based on the QR algorithm and therefore solves for all eigenvalues and eigenvectors simultaneously.

Finally, for each frequency ω, the eigenvalue with the largest spatial growth rate is extracted from the calculations, since we assume that only the most amplified wavenumber is observed in the experiments. This hypothesis is supported by the fact that in the experiments the phase speed for each excitation frequency is constant, indicating one single (and constant) wavelength. The growth rate of the most amplified wavelength is plotted as a function of the frequency, and compared with the experimental growth rates.

3.2.1. *Boundary conditions on the interface*

To close the two sets of equations presented in the previous section, we need to couple the velocities and pressures in the different phases together. These coupling conditions are derived from the flow physics.

The boundary conditions for the total flow field at the interface between gas and liquid are, in dimensional form:

(i–ii) all velocity components are continuous at the interface:

$$\boldsymbol{U}^*_{l,tot} = \boldsymbol{U}^*_{g,tot}, \tag{3.25}$$

(iii) the tangential stresses are continuous at the interface:

$$\boldsymbol{n}^*_{tot} \times (\tau^*_{l,tot} - \tau^*_{g,tot}) \cdot \boldsymbol{n}^*_{tot} = 0, \tag{3.26}$$

and

(iv) there is a surface tension induced jump in the normal stress:

$$\boldsymbol{n}^*_{tot} \cdot (\tau^*_{l,tot} - \tau^*_{g,tot}) \cdot \boldsymbol{n}^*_{tot} = -\gamma s^*_{tot}, \tag{3.27}$$

where γ is the surface tension coefficient, $\boldsymbol{n}^*_{tot}$ is the surface normal, $\tau^*_{p,tot}$ is the total stress tensor with pressure included, and s^*_{tot} is the total surface divergence operator defined as

$$s^*_{tot} = (\nabla \cdot \boldsymbol{n}^*_{tot})\boldsymbol{n}^*_{tot}. \tag{3.28}$$

Here, the direction of the surface normal $\boldsymbol{n}^*_{tot}$ is given by the location of the interface H_{tot}, and thus we also need an equation for H_{tot}. This comes from the assumption that the sheet-normal displacement of the interface follows the sheet-normal displacement of a fluid particle on the interface:

$$\frac{\partial H^*_{tot}}{\partial t} + (\boldsymbol{U}^*_{tot} \cdot \nabla) H^*_{tot} = V^*_{tot}. \tag{3.29}$$

To non-dimensionalize the boundary conditions with liquid quantities, as before, we need We (3.2), $\tilde{\rho}$ (3.3) and $\tilde{\mu}$ (3.4).

Similar to the other variables, we introduce a division of the interface position into a steady and oscillating part as $H^*_{tot} = H^* + \hat{h}\,\mathrm{e}^{\mathrm{i}(\alpha x - \omega t)}$. After some algebra, the linearized non-dimensional boundary conditions become (for details, see Söderberg & Alfredsson 1998):

(i–ii) velocity continuity on the free surface (cf. (3.25)):

$$D\hat{v}_l - \mathrm{i}\alpha\hat{h}(DU_l - DU_g) = D\hat{v}_g, \tag{3.30}$$

$$\hat{v}_l = \hat{v}_g, \tag{3.31}$$

where (3.30) is the continuity of $\hat{u}$ transformed to a condition for $\hat{v}$ using (3.21),

(iii) continuity of the tangential stress (cf. (3.26)):

$$(D^2 + \alpha^2)\hat{v}_l - \mathrm{i}\alpha\hat{h}(D^2U_l - \tilde{\mu}D^2U_g) = \tilde{\mu}(D^2 + \alpha^2)\hat{v}_g, \tag{3.32}$$

(iv) surface-tension-induced jump of the normal stress (cf. (3.27)):

$$\begin{aligned}&\left[(\mathrm{i}\alpha U_l - \mathrm{i}\omega) - Re_l^{-1}(D^2 - 3\alpha^2)\right] D\hat{v}_l - \mathrm{i}\alpha DU_l\hat{v}_l \\ &\quad = \left[\tilde{\rho}(\mathrm{i}\alpha U_g - \mathrm{i}\omega) - \tilde{\mu}Re_l^{-1}(D^2 - 3\alpha^2)\right] D\hat{v}_g - \mathrm{i}\alpha\tilde{\rho}DU_g\hat{v}_g - We^{-1}\alpha^4\hat{h},\end{aligned} \tag{3.33}$$

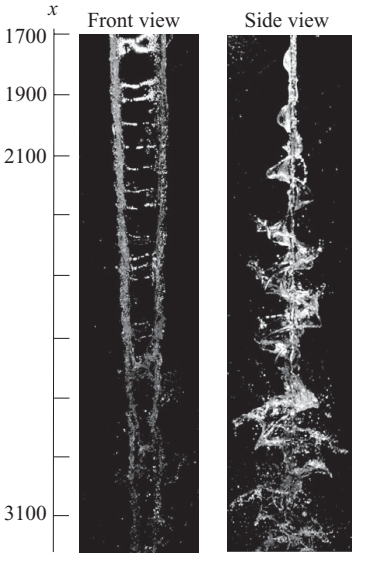

FIGURE 13. The natural oscillation of the water sheet in stagnant air ($x = 1700$–3200 measured from the nozzle exit), $Re_l \approx 3000$ and $We \approx 350$.

and

(v) interface equation of motion:

$$-\mathrm{i}\omega\hat{h} + U\frac{\partial \hat{h}}{\partial x} = \hat{v}. \tag{3.34}$$

4. Experimental results and comparison with theory

4.1. *A plane liquid jet into stagnant air*

The visualisations shown in this section were performed with a prototype jet facility with 150 mm width for the water sheet and no air flow nozzles. In figure 13, the sheet is shown in the xz (front) and xy (side) planes. The oscillations of the sheet are directly seen in the side view (right photograph) and as variations of the reflected light in the front view (left). The front view also shows that under natural conditions without forcing, the disturbances developing on the sheet are distinctively two-dimensional and independent of z. This can be concluded from the horizontal nature of the reflections in the sheet. From the side view, it is clear that the dominant oscillation is sinusoidal.

If the flow instead is disturbed at a given frequency with the loudspeakers, the sheet picks up this frequency. This is illustrated in figure 14(*a,b*), where front and side views for frequencies $f^* = 110$ and 150 Hz are shown, respectively. First, it is noted that the irregular oscillations of figure 13 are replaced by oscillations with a well-defined wavelength. The reflections in the front views again show a distinct two-dimensionality of the disturbances and it is also seen that the wavelength is shorter for the higher frequency. Furthermore, the side views show that the disturbances are sinusoidal and the growth is considerably stronger for 110 Hz (figure 14*a*) than for 150 Hz (figure 14*b*).

The disturbance growth rate is quantified by looking at the root mean square of the surface angle (θ_{rms}) at different streamwise positions (cf. figure 4). An example of such

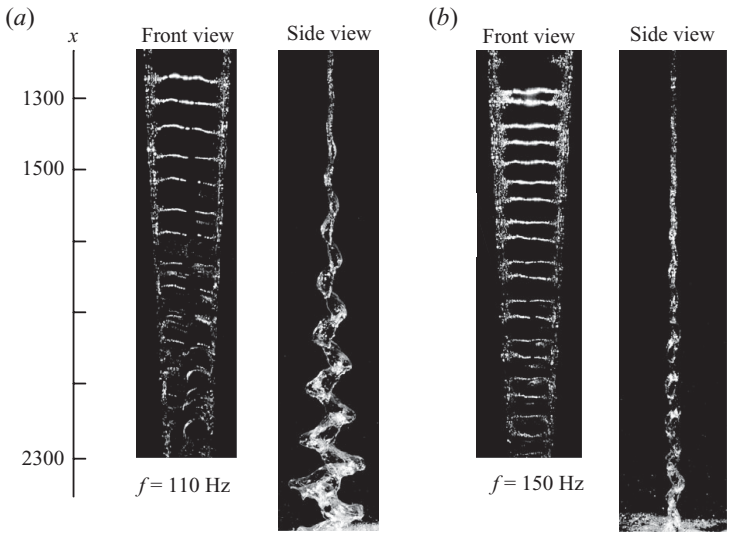

FIGURE 14. The forced water sheet oscillation for two different excitation frequencies: 110 Hz (*a*) and 150 Hz (*b*).

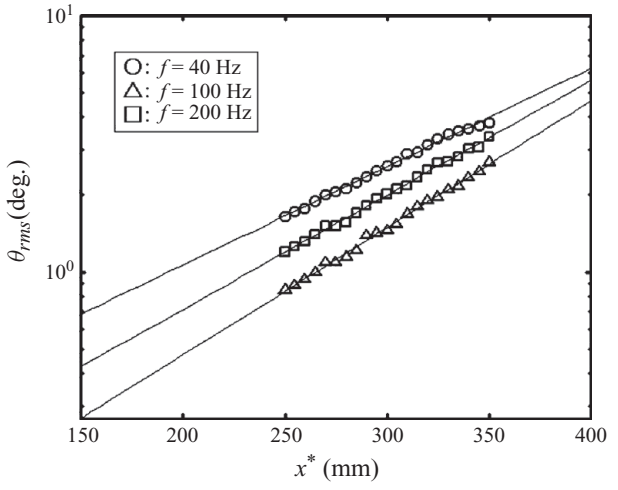

FIGURE 15. The amplitude of the disturbance in the region $x^* = 250$–350 mm (non-dimensional, $x \approx 500$–700).

curves for three different frequencies is shown in figure 15. The root mean square of θ is seen to grow exponentially and for each frequency, a growth factor can be readily determined as the slope of the respective line. The surface oscillation amplitude h has the same exponential growth rate. Note that the initial disturbance amplitude varies depending both on the exact level of forcing and receptivity, and only the growth rate is of interest in our analysis. Note that the fact that the sheet picks up the disturbance frequency and amplifies it with a distinct growth rate demonstrates that the disturbances are of a convective nature, and can be analysed by the local spatial approach used in this work. Furthermore, the angular phase of the measured wave in different streamwise positions showed that the phase speed of the disturbances is constant and equal to the water velocity, a feature that is confirmed by the linear

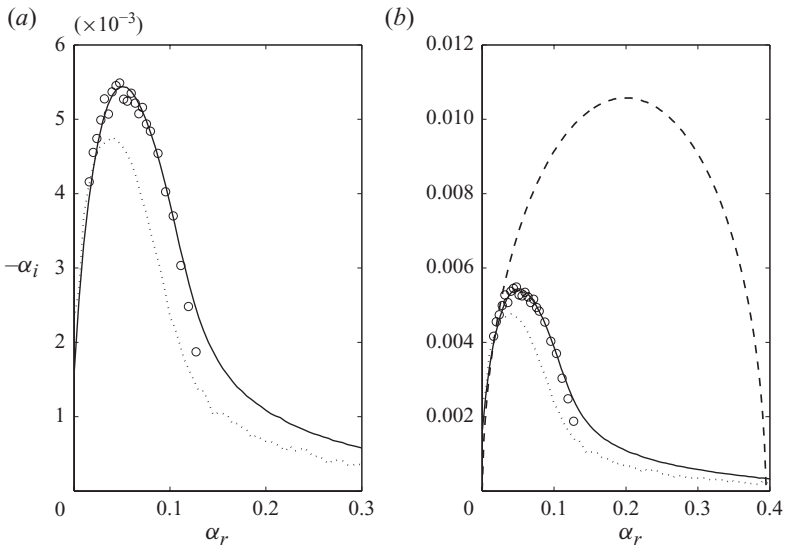

FIGURE 16. (*a*) The experimental (○) and theoretical spatial growth rates as functions of wavenumber in stagnant air ($Re_l = 2910$, $We = 350$): Stokes model (solid line) and Sakiadis model (dotted line). The computations are performed in the middle of the measurement interval, at $x = 600$, using the nozzle outlet as a virtual leading edge for both models. (*b*) All three growth rate curves compared to a solution where air is assumed inviscid (Li 1993, dashed line). The inviscid solution clearly overestimates the experimentally observed growth rates and wavelengths, whereas the viscous solutions are in good agreement.

stability analysis. Note that the growth rates for curves such as those in figure 15 were obtained further upstream (and thus at lower disturbance amplitudes) than the visualisations in figure 14. This was to ensure that the measurements were taken in the regime of linear growth, while it was difficult to obtain visualisations where the disturbance amplitude was very small.

Experimental growth rates are compared with theoretical ones for the Stokes and Sakiadis boundary layer models in figure 16(*a*). The spatial growth rate $-\alpha_i$ is shown as a function of the wavenumber α_r. At each real frequency ω, a spectrum of α is calculated and the one with largest growth (largest $-\alpha_i$) is plotted in the figure; the curve is obtained by performing the eigenvalue analysis for a sequence of ω. Since the experiments are measured over an interval in the spanwise direction while the theoretical analysis is local, a choice regarding the position at which to perform the analysis has to be made. Here, the centre of the interval used in measurements was chosen. For the experimental values, the spatial growth rate is obtained from lines similar to the those in figure 15 and the wavenumber is given by the frequency and the velocity of the sheet (i.e. the phase speed as discussed above).

The comparison in stagnant air yields excellent agreement for the Stokes boundary-layer model as seen in figure 16(*a*). The experimental data (circles) follow the theoretical curve (solid line) over the peak, until it falls slightly below at $\alpha_r = 0.12$. Higher frequencies could not be measured at the same x-position due to the low amplitude. For the Sakiadis model (dotted line), the agreement is no more than satisfactory. In figure 16(*b*) the results are drawn together with the analytic solution assuming inviscid air by Li (1993) (dashed line), obtained from the expression given in Appendix A. The inviscid solution overestimates the growth rate and wavenumber

of the peak by a factor of 2–3, while the viscous solutions reproduce the experimental behaviour.

The difference between Stokes and Sakiadis models is distinct although not substantial and shows the relative importance of correct models for the boundary layer in the air in order to pinpoint the growth rate exactly. Even though the Sakiadis model includes more physics (specifically the development in the streamwise direction) than the somewhat *ad hoc* Stokes model, the latter compares better with the experiments. This could be a result of the fact that there are aspects of the air flow, such as the inevitable re-circulation in the room, that neither the Stokes nor the Sakiadis model account for. However, it will be shown later that for the same characteristic parameters (boundary-layer thickness or shear from air at the interface), both models produce nearly identical results, and therefore a correct choice of these for the measurement position under study should be more important than the choice of the model.

It should be noted that no parameters have been adjusted for the comparison; the physical constants are extracted from tables using the measured mean temperature for water and air, and the air boundary-layer profiles computed by taking the middle of the measurement interval as the distance from the virtual leading edge for both models. Since the water profile has boundary layers at the nozzle exit, there is a reason to believe that the streamwise development of the air boundary layer is delayed. If the virtual leading edge is actually located downstream from the outlet, this would explain why the Sakiadis model somewhat underestimates the growth rates.

4.2. *A plane liquid jet with confluent air*

To visualize the effect of gas flow the whole way from the nozzle to breakup, some initial experiments were performed without the guiding walls and thus without suction for the air flow around the water sheet. Although the uniformity of the air flow profile was not as good as in the later experiments with walls, the pictures provide a good qualitative measure of how blowing air in parallel to the liquid sheet affects the stability.

The oscillating liquid sheet with different amounts of air co-flow is seen in figure 17. The non-dimensional gas velocity is varied between $U_g^\infty = 0$ and $U_g^\infty = 7/3$. It is clear that the air co-flow has a considerable effect on the stability. Going from the stagnant case $U_g^\infty = 0$ to $U_g^\infty = 5/6$, the oscillation is almost totally suppressed. When the gas velocity is increased above the liquid velocity, the sheet destabilizes again. This is consistent with previous and present theoretical findings (see §§ 1 and 5.2). The liquid sheet seems to be slightly more unstable and have a more irregular shape for overflow ($U_g^\infty > 1$), but this might be an effect of difficulties to control the air flow distribution in the overflow case. For the same reason, experimental growth rates will be presented only for $U_g^\infty < 1$.

The second visualisation concentrating on the breakup process (figure 18) is made in the current experimental set-up. With the walls, it is not possible to observe the whole wave growth process. However, the breakup is seen to be delayed considerably, when air flow velocity is increased from 0 (stagnant air) to half of the liquid velocity.

The growth rates for six different forcing frequencies are seen in figure 19, for three values of the gas velocity: $U_g^\infty = 0$, 0.3 and 0.5. While the shapes of the growth rate curves are similar, the liquid sheet becomes less unstable for all frequencies by the gas flow. The agreement in the stagnant case is good, but not as excellent as in the previous section, probably because the measurement region is longer ($x = 468$–755),

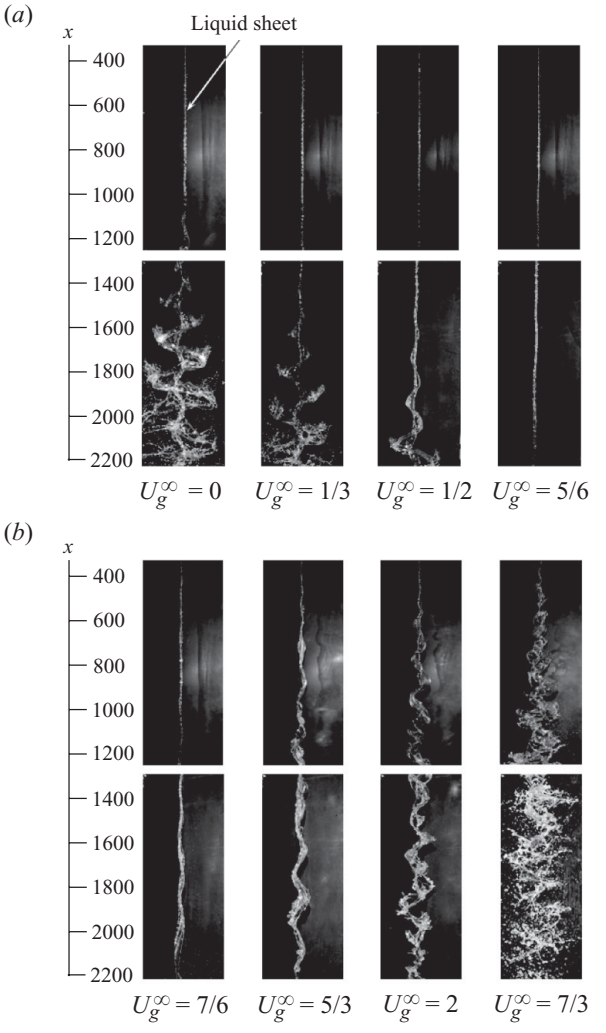

FIGURE 17. (*a, b*) Visualisation of the liquid jet over a long distance without guiding walls for the air flow, for different gas blowing velocities.

and therefore the experimental growth rates are averaged over a longer streamwise interval.

When confluent air is considered, the computed solution also predicts the trends seen in the experiments. In the same figure, the computed growth rate curves from the Stokes' model are drawn with solid lines. The air flow has a stabilizing effect for all frequencies, and the peak growth rates are within 10 % relative and 0.4×10^{-3} absolute accuracy. Sometimes the theory slightly overpredicts, sometimes underpredicts the experimental growth rates. One reason might be that it is difficult to obtain a homogeneous air flow when blowing, due to the inclination of the air flow nozzles, as indicated in the previous section (figure 7). Also, small modelling errors, such as the uncertainty in temperature that affects the values of Re and We, and the shape of the velocity profiles for both water and air, contribute to the difference.

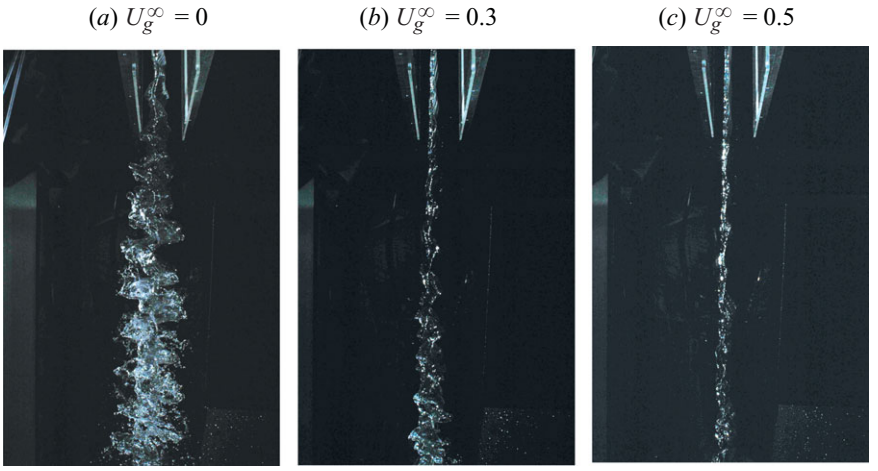

FIGURE 18. (Colour online) (*a–c*) Visualisation of the breakup process, far from the inlet, with guiding walls guaranteeing uniform air flow, for different gas blowing velocities.

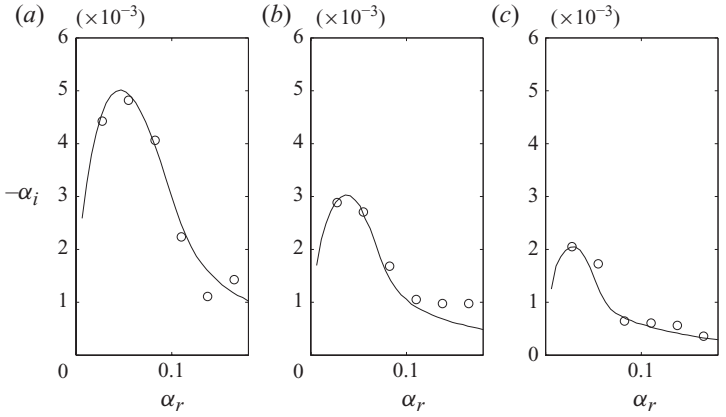

FIGURE 19. The experimental (○) and theoretical (—) spatial stability results ($Re_l = 3170$, $We = 312$, Stokes model), with different gas co-blowing velocities: (*a*) $U_g^\infty = 0$, (*b*) $U_g^\infty = 0.3$ and (*c*) $U_g^\infty = 0.5$.

5. Theoretical consideration

On the basis of the inviscid studies, we expect the relative velocity between gas and liquid to be one important parameter, but we are also looking for viscous parameters that would quantify the difference from the inviscid result. The air boundary-layer thickness δ represents the global scale of a viscous modification, and the shear at the liquid surface σ is a local scale near the surface.

5.1. *Liquid jet in the stagnant air*

In figure 20 eigenvalue curves in stagnant air ($U_g^\infty = 0$) are shown for different streamwise positions, for the Stokes (figure 20*a*) and Sakiadis (figure 20*b*) boundary-layer models. The results for the two models share several common features. It is clearly seen that for both cases the growth rate of the most unstable mode and its wavenumber decrease when going downstream. This decrease is most pronounced

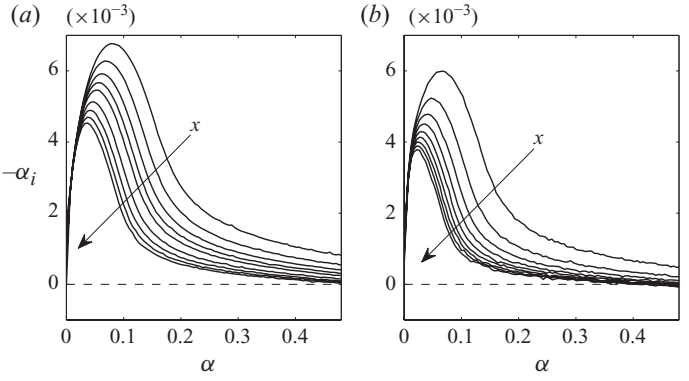

FIGURE 20. Growth rate curves at $Re = 3200$ and $We = 340$ from the (a) Stokes and (b) Sakiadis air flow models, $U_g^\infty = 0$, for different streamwise positions: $x = 200, 400, 600, \ldots, 1800$. In both cases, the peak moves towards longer wavelengths and the growth rate decreases downstream.

for the upstream x-positions, while the curves for the downstream positions are near each other. The appearance of the whole eigenvalue curve is similar.

The most unstable wavenumber for each x-position (position of the peak) and its growth rate (height of the peak) differ by 5 %–10 % between the two models in the streamwise region under study, starting from $x = 200$, which corresponds to a distance of 10 cm from the nozzle exit in the experiments. Recall that, as shown in figure 9, the viscous parameters (δ and σ) at a given streamwise position have both slightly larger absolute value for the Sakiadis than for the Stokes model.

The stabilisation of the sheet with the viscous development of the base flow is expected already from an inviscid stability analysis, since the vorticity thickness of the air increases. Since the basic instability mechanism of the liquid sheet is the same as for the Kelvin–Helmholtz instability of a vortex sheet (Chandrasekhar 1961), the stabilisation can be seen as an analogy to the classical piece-wise mixing layer: it is known that the stability curve of a piece-wise mixing layer deviates from the linear Kelvin–Helmholtz curve at a cutoff wavenumber inversely proportional to the vorticity thickness. However, this comparison should not be taken too far, since the liquid sheet problem involves more physics; even the appearance of the inviscid curve without taking the vorticity thickness into account is fundamentally different from the Kelvin–Helmholtz curve.

Indeed, the growth rate seems to be inversely proportional to the square root of δ, or directly proportional to the square root of σ. In figure 21, the growth and wavenumber for both cases are compared as functions of $|\sigma|^{1/2}$ and $\delta^{-1/2}$. In these scalings, the two models almost collapse. In particular, the growth rate displays a linear dependence on $|\sigma|^{1/2}$ in figure 21(d). In figures 21(a) and 21(c), the wavenumber also seems to have a linear dependence on the same quantities, although it is obvious from the figure that the slope cannot stay constant when $\delta \to \infty$.

5.2. *Effect of gas flow on disturbance growth*

The inviscid instability of a liquid sheet is known to be of aerodynamic nature. The co-flow of gas stabilizes the sheet, if the relative speed between gas and liquid is decreased. In other words, an increasing gas free-stream velocity U_g^∞ leads to a more stable sheet to the point where gas velocity is equal to liquid velocity ($U_g = 1$), in

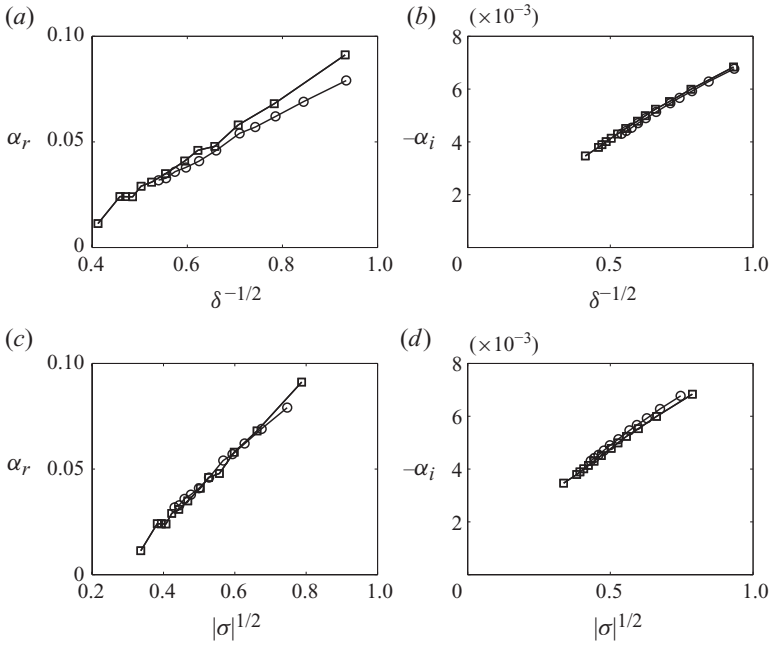

FIGURE 21. The peak eigenvalues for each x-position ($x = 200, 400, 600, \ldots, 1800$) from figure 20 for Stokes (-○-) and Sakiadis (-□-) as functions of $\delta^{-1/2}$ and $|\sigma|^{1/2}$: (a) most unstable wavenumber α_r against inverse square root of the boundary-layer thickness $\delta^{-1/2}$; (b) growth rate $-\alpha_i$ against $\delta^{-1/2}$; (c) most unstable wavenumber against $|\sigma|^{1/2}$; (d) growth rate against $|\sigma|^{1/2}$.

which case the sheet is stable. When the gas velocity is increased over the liquid velocity, the sheet destabilizes again.

This feature is clearly seen in the eigenvalue curves from the Stokes and Sakiadis models in figure 22. For the Stokes model in figure 22(a,c), the difference between $U_g^\infty - 1 = 1$ and $U_g^\infty - 1 = -1$ is only 5 %, so the curves are nearly symmetric with respect to the velocity difference. For the Sakiadis model in figure 22(b,d), the same difference is 17 %. The reason can be understood by looking at the base flow profiles in figure 10 and the development of δ and σ for different U_g^∞ in figure 11. For the Stokes model, the parameters are symmetric with respect to $(U_g^\infty - 1)$, but for the Sakiadis model asymmetric. Although measurements were not made for $U_g^\infty > 1$, the visualisations in figure 17 give some support to the Sakiadis result in this case, since the wave growth seems to be faster for the overblowing case. However, it has to be kept in mind that this particular visualisation was made without the guiding vanes guaranteeing uniform air flow.

The growth rate of the most unstable mode as a function of the relative velocity $U_g^\infty - 1$ is seen for both models in figure 23. Dependence on this parameter is expected from the inviscid analysis, as for Kelvin–Helmholtz-type instability. In the inviscid analysis, the dependence on the growth rate of $U_g^\infty - 1$ can be shown to be quadratic – the growth rate curve based on uniform velocity in water and air is shown by the dotted curve in the same figure, and derived in Appendix B. In our study, the growth rate scales linearly for $|U_g^\infty - 1| \geqslant 0.4$ and the best fit is shown by a line in the figure together with the data points. A similar deviation from the inviscid analysis was noticed in the viscous analysis of Lozano *et al.* (2001), who looked at the frequency

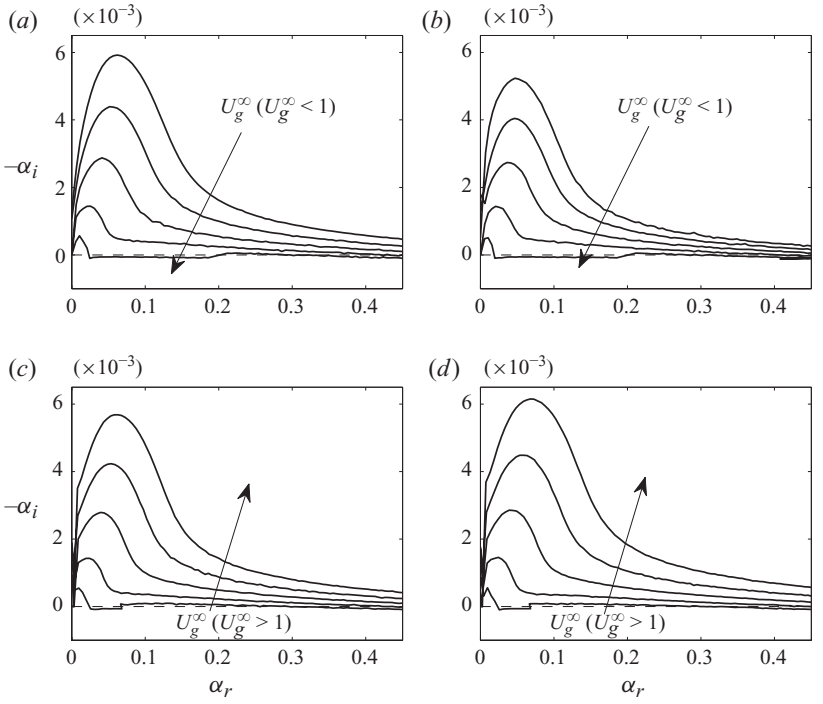

FIGURE 22. Growth rate curves (at $Re = 3200$, $We = 340$, $x = 200$) for different air velocities, (*a*) Stokes, $U_g^\infty = 0$, 0.2, 0.4, 0.6, 0.8 ($U_g^\infty < 1$); (*b*) Sakiadis, $U_g^\infty = 0$, 0.2, 0.4, 0.6, 0.8 ($U_g^\infty < 1$); (*c*) Stokes, $U_g^\infty = 1.2$, 1.4, 1.6, 1.8, 2 ($U_g^\infty > 1$); (*d*) Sakiadis, $U_g^\infty = 1.2$, 1.4, 1.6, 1.8, 2 ($U_g^\infty > 1$). Increasing air velocity stabilizes if $U_g^\infty \leqslant 1$, and destabilizes otherwise.

for the most unstable mode as a function of air velocity – the frequency increased linearly, instead of a quadratic dependence predicted by the inviscid analysis.

The slopes of the lines for Sakiadis model (solid) are different for negative ($U_g^\infty < 1$) and positive velocity differences, with $U_g^\infty > 1$ being slightly more unstable. For Stokes model (dashed), the same linear dependency is seen, but the slopes are symmetric with respect to the velocity difference. For all cases, the lines in figure 23 intersect at a point in the region $|U_g^\infty| = 0.3$–0.4. The data points at $|U_g^\infty - 1| = \pm 0.2$ that were not used for the linear fit are all above their respective lines. The intersection of the lines and deviation from the linear fit for low-velocity differences is an interesting feature. It is natural to believe that for these very long waves, the viscous and inviscid solutions approach each other, i.e. the Kelvin–Helmholtz instability mechanism gradually weakens and is overtaken by neutrally stable capillary waves. We also note that there is more scattering in the eigenvalues for $|U_g^\infty - 1| = 0.2$ than at larger velocity differences.

Furthermore, the slopes of the lines in figure 23 decrease with the streamwise position. However, the linear relation persists. This is only possible if the dependence of the growth rate on the x-position is of the same form for different blowing velocities. Figure 24 confirms that there is a nearly linear scaling with $|\sigma|^{1/2}$ for blowing velocities that differ from the liquid velocity by a factor larger than or equal to 0.4, as in the stagnant air case. Again, if the profiles with the same characteristic parameters are considered, the difference between Sakiadis and Stokes is very small. Moreover, when the data are drawn as a function of $\sigma^{1/2}$ like in this figure, especially for the Sakiadis case, points with the same absolute velocity difference ($|U_g^\infty - 1|$) for

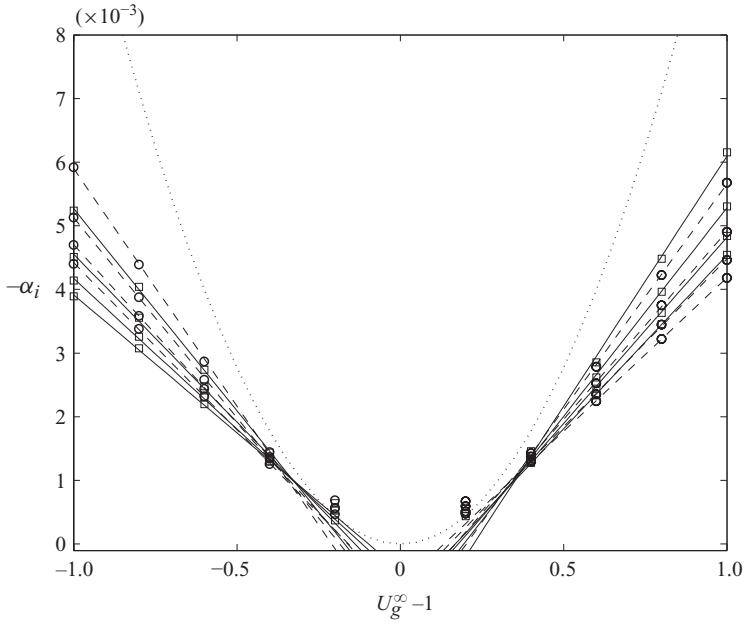

FIGURE 23. The largest growth rate at $Re = 3200$, $We = 340$ as a function of the velocity difference $U_g^\infty - 1$ at different x-positions ($x = 0.2, 0.4, 0.6, 0.8$) for the Sakiadis (—□—) and Stokes (- -○- -) models. The markers represent calculated values, while lines are linear fits for $|U_g^\infty| > 0.4$. A temporal solution assuming inviscid air and water is given by the dotted curve.

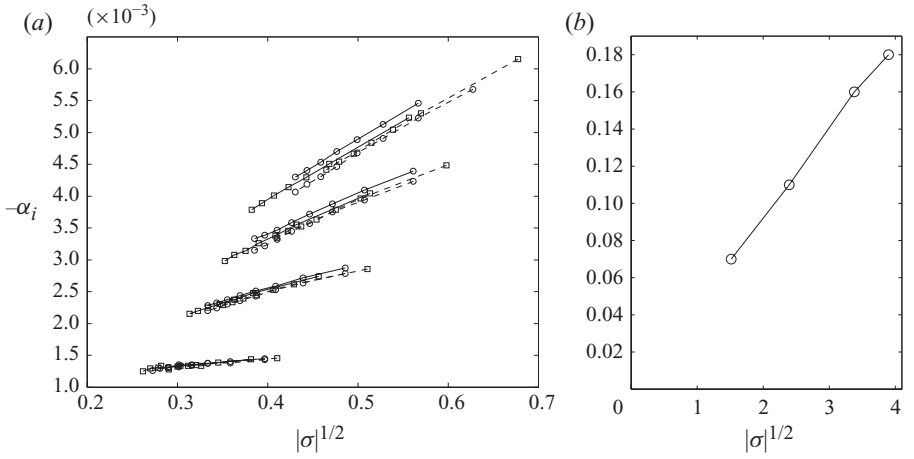

FIGURE 24. (*a*) The growth rate of the peak eigenvalues for different x-positions ($x = 400$, 800, 1000, 1200, 1400, 1600, 1800) for the Stokes and Sakiadis models as functions of $|\sigma|^{1/2}$, from up and down: —□—, Sakiadis ($U_g^\infty = 0, 0.2, 0.4, 0.6$); —○—, Stokes ($U_g^\infty = 0, 0.2, 0.4, 0.6$); - -□- -, Sakiadis ($U_g^\infty = 2, 1.8, 1.6, 1.4$); - -○- -, Stokes ($U_g^\infty = 2, 1.8, 1.6, 1.4$). (*b*) The same scaling extracted from the data in Lozano *et al.* (2001) for $U_g^\infty = 12.5$, $Re_l = 340$, and a different base flow model.

both underflow and overflow line up on the same line. This was not as obvious if $\delta^{-1/2}$ was considered. Therefore, we consider $\sigma^{1/2}$ to be the most attractive parameter to quantify the viscous scaling.

Remarkably, we could find the same viscous scaling from the literature, by extracting the maxima from the temporal growth rate curves drawn as a function of air boundary-layer thickness in figure 7 of Lozano *et al.* (2001). Their base flow model and parameter region are completely different. Their non-dimensional gas velocity (in our coordinates) is $U_g^\infty = 12.5$, and water Reynolds number $Re_l = 340$. The scaling is shown in figure 24(*b*). The derivation of σ for the model of Lozano *et al.* (2001) is given in Appendix C.

When it comes to the wavenumbers for different U_g^∞, we could not find universal scaling laws. One reason might be that the plateau in the growth rate curves is rather flat, making the uncertainty in the wavenumber bigger than that in the growth rate. However, for $U_g^\infty > 1$ both models seem to approach a linear dependency between shear and wavenumber, the latter exchangeable to frequency in our case, which is consistent with the experimental and numerical results of Lozano *et al.* (2001) for high blowing velocities.

6. Conclusions

The disturbance growth for plane liquid sheets with air co-flow has been analysed experimentally and theoretically. Unlike many other studies, which have a rapid breakup as a goal, our aim is to quantify the stabilizing effect of an air flow with a similar speed as the liquid flow.

Experiments have been conducted for a water sheet ($Re_l \approx 3000$, $We \approx 300$), both in stagnant air and with different amounts of co-flow. The liquid sheet was excited with different frequencies by acoustic forcing at the nozzle exit. The time-varying inclination of the water surface was measured at different streamwise positions. With this method, we could extract the spatial growth rate along with the frequency of the waves.

A linear spatial stability analysis has been made using two different air flow models – the theoretically correct Sakiadis model obtained by solving the boundary-layer similarity equations, and an analytical Stokes model based on Stokes' solution of the flow above an instantaneously started plate, where the time dependency was changed to an x-dependency. The liquid velocity was assumed to be uniform.

It was shown that the dependence of the growth rate on the inviscid stability parameter – relative velocity between air and water – is retained for viscous gas, even if the viscous growth rates can be smaller by several orders of magnitude. The dependence of this parameter is approximately linear, instead of a quadratic dependence predicted by a fully inviscid analysis. The two boundary-layer models were shown to produce very similar results, which justifies the use of Stokes model in other (Söderberg & Alfredsson 1998; Söderberg 2003) and future studies. The viscous effect was investigated in terms of two parameters – δ, the boundary-layer thickness for the air flow quantifying the scale of the total viscous modification, and σ, the shear from air at the interface representing the viscous effect near the surface. As a function of these parameters, both models nearly collapse and show a linear dependence between the growth rate and the square root of $|\sigma|$ starting some distance downstream from the nozzle exit.

The Stokes model was compared with experiments. The results are in very good agreement for the stagnant air case, while the previous inviscid solution of Li (1993) overestimates the most unstable wavenumber and its growth rate by more than a factor of 2. For the case of air co-flow, the trends are the same, and the quantitative agreement between experiments and theory is also very good, but not perfect. We believe this is due to experimental uncertainties concerning both the exact shape and magnitude of the air flow and the non-dimensional numbers involved.

In the theoretical studies, the Stokes model gives an almost symmetric growth rate curve with respect to velocity difference, irrespective of the application of underflow ($U_g^\infty < 1$) or overflow ($U_g^\infty > 1$). For the more physical Sakiadis model, the slope is changed if overflow is applied. At this point, experimental growth rates have not been obtained for $U_g^\infty > 1$ and the experimental confirmation of this has to be left for a future study. A linear dependence between the growth rate and $U_g^\infty - 1$ is obtained for both cases for $|U_g^\infty - 1| > 0.4$. As functions of σ or δ, the models collapse. This means that for the same σ, the influence of velocity difference is symmetric. Therefore, this leaves us with two parameters: absolute value of the velocity difference $|U_g^\infty - 1|$ (inviscid) and shear from air at the surface σ (viscous).

Since the viscous parameter σ also changes with gas velocity, it would be tempting to try to characterise the stability in terms of this parameter only. Our results show that for different values of $U_g^\infty - 1$, the same shear at the surface leads to different growth rates, underlining the importance of the inviscid parameter. However, when $U_g^\infty - 1$ is kept constant, the same linear dependence on $|\sigma|^{1/2}$ is obtained for the two different boundary-layer models, and also extracted from a previous result found in the literature with a strong overflow in air.

In future work, it would be interesting to test the validity of these scalings experimentally. In order to do this, it is crucial to accurately measure the air (and water) boundary-layer profile at different streamwise positions. Also, it could be interesting to repeat the theoretical analysis using inviscid stability in air but taking into account the vorticity thickness of the air boundary layer. The aim would be to determine if the viscous stabilisation can be explained by the base flow modification alone. Alternatively, a complete viscous stability analysis (as presented here) is necessary.

The authors gratefully thank Masamichi Tosaki, Yuta Wakabayashi and Akihiko Mori for their support in arranging the water jet facility and the experiments.

Appendix A. Spatial stability of a viscous liquid sheet in an inviscid stagnant gas

A previous solution assuming viscous liquid and inviscid gas is compared with our experiments and numerical solution with viscous gas in figure 16. The dispersion relation for sinuous disturbances is given by (5) in Li (1993):

$$\left[(m-\Omega) - \mathrm{i}\frac{4m^2}{R}\right](m-\Omega)\tanh(m) + \frac{4m^3}{R^2}[S\tanh(S) - m\tanh(m)] + \rho\Omega^2 - \frac{m^3}{\beta^2} = 0, \quad \text{(A 1)}$$

where $m = k^* a^*$, $\Omega = \omega^* a^*/U^*$, $\beta = We^{1/2} = U^*/(\sigma^* a^* \rho_l^*)^{1/2}$, $\rho = \rho_g^*/\rho_l^*$, $R = \rho_l^* U^* a^*/\mu_l^*$ and $S = [m^2 + \mathrm{i}R(m-\Omega)]^{1/2}$.

The solution for our parameter values can be obtained by making the substitutions: $m = \alpha$, $\Omega = \omega$, $\beta = We^{1/2}$, $R = Re_l$.

Appendix B. Fully inviscid temporal stability of a liquid sheet in a confluent gas

The derivation here is based on the solution of Squire (1953) for an inviscid liquid sheet in inviscid stagnant gas, both with uniform velocity profiles. For the case of long waves compared to the thickness of the liquid sheet, one recovers maximum of

the dimensional growth rate:

$$\omega^*_{i,max} = \frac{\tilde{\rho} U_l^{*2}}{2\sqrt{\dfrac{\gamma^* h^*}{\rho_l^*}}}. \tag{B 1}$$

Since in the inviscid equations there is a slip boundary condition, they can be translated without affecting the sheet-normal velocity of the disturbance, and thus the growth rate. The only quantity with the streamwise velocity U^* that will appear in the equations and boundary conditions is $\alpha^* U - \omega^*$. Consequently, if we transform the equations into a coordinate system in which the gas is stagnant, $\tilde{U}^* = U^* - U_g^*$, the maximal growth rate will have the same value as in the untransformed system, as will the wavenumber α^*_{max} for which this growth rate occurs. The frequency, however, will be shifted by an amount of $\alpha^*_{max} U_g$, since the phase velocity is shifted by U_g^*.

The dimensional growth rate in our case is, consequently,

$$\omega^*_{i,max} = \frac{\tilde{\rho}(U_l^* - U_g^*)^2}{2\sqrt{\dfrac{\gamma^* h^*}{\rho_l^*}}}. \tag{B 2}$$

The non-dimensional growth rate in our system becomes

$$\omega_{i,max} = \frac{h^*}{U_l^*} \frac{\tilde{\rho}(U_l^* - U_g^*)^2}{2\sqrt{\dfrac{\gamma^* h^*}{\rho_l^*}}} = \frac{1}{2}\tilde{\rho}(U_g - 1)^2 \sqrt{We}. \tag{B 3}$$

To convert between the temporal and spatial formulations, we also need to approximate the phase velocity. We get from Squire (1953), for stagnant air,

$$c^*_{r,max} = \frac{U_l^*}{1 + \tilde{\rho}\coth(\alpha h)} \approx U_l^* \tag{B 4}$$

for water in air. Applying the transformation to get the solution in moving air, and shifting the phase velocity by U_g^*, we simply get

$$c^*_{r,max} = (U_l^* - U_g^*) + U_g^* = U_l^* \tag{B 5}$$

or in non-dimensional formulation

$$c_{r,max} = 1. \tag{B 6}$$

Appendix C. Derivation of shear at the surface for the model of Lozano *et al.* 2001

The dimensional velocity profile of Lozano *et al.* (2001) in air is

$$U_2^*(y^*) = b_0^* + b_1^* \frac{(y^* - h^*)}{\delta^*} + b_2^* \left(\frac{(y^* - h^*)}{\delta^*}\right)^2, \tag{C 1}$$

where b_0^*, b_1^* and b_2^* are constants (dependent on δ^*).
The dimensional y^*-derivative of this becomes

$$\frac{\mathrm{d}U_2^*}{\mathrm{d}y^*} = \frac{b_1^*}{\delta^*} + \frac{2b_2^*}{\delta^*}\frac{(y^* - h^*)}{\delta^*}, \tag{C 2}$$

of which the second term vanishes on the interface between water and air at $y^* = h^*$. The non-dimensional form of this at the interface ($y = 1$) becomes

$$\frac{\mathrm{d}U_2}{\mathrm{d}y}(y=1) = \frac{b_1^* h^*}{\langle U_1^* \rangle \delta^*} = \frac{b_1^*}{\langle U_1^* \rangle \delta}, \tag{C 3}$$

where the vertical mean of the water velocity $\langle U_1^* \rangle$ is the velocity scale and h^* is the length scale. It is given that

$$b_1^* = (U_2^{*\infty} - \langle U_1^* \rangle) \frac{\delta^*}{h^* \left(2/3\mu_r + \dfrac{\delta^*}{h^*} \right)} = \left(U_2^{*\infty} - U_1^* \right) \frac{\delta}{(2/3\mu_r + \delta)} \tag{C 4}$$

and μ_r is the air/water viscosity ratio.
Finally,

$$\sigma = \frac{\mathrm{d}U_2}{\mathrm{d}y}(y=1) = \frac{\left(U_2^{\infty} - 1 \right)}{(2/3\mu_r + \delta)}. \tag{C 5}$$

Since $\mu_r \approx 0.01$, this implies in practice that $\delta \sim 1/\sigma$.

REFERENCES

Chandrasekhar, S. 1961 *Hydrodynamic and Hydromagnetic Stability*, 3rd edn. Dover.

Eggers, J. & Villermaux, E. 2008 Physics of liquid jets. *Rep. Prog. Phys.* **71**, 036601.

Hagerty, W. W. & Shea, J. F. 1955 A study of the stability of plane fluid sheets. *J. Appl. Mech.* **22**, 509–514.

Li, X. 1993 Spatial instability of plane liquid sheets. *Chem. Engng Sci.* **48** (16), 2973–2981.

Li, X. & Tankin, R. S. 1991 On the temporal instability of a two-dimensional viscous liquid sheet. *J. Fluid Mech.* **226**, 425–443.

Lozano, A., Barreras, F., Hauke, G. & Dopazo, C. 2001 Longitudinal instabilities in an air-blasted liquid sheet. *J. Fluid Mech.* **437**, 143–173.

Mansour, A. & Chigier, N. 1991 Dynamic behavior of liquid sheets. *Phys. Fluids* A **3**, 2971–2980.

Park, J., Huh, K. Y., Li, X. & Renksizbulut, M. 2004 Experimental investigation on cellular breakup of a planar liquid sheet from an air-blast nozzle. *Phys. Fluids* **16** (3), 625–632.

Rayleigh, Lord 1878 On the instability of jets. *Proc. Lond. Math. Soc.* **10** (1), 4–13.

Sakiadis, B. C. 1961*a* Boundary-layer behaviour on continuous solid surfaces. I. Boundary-layer equations for two-dimensional and axisymmetric flow. *AIChe J.* **7** (1), 26–28.

Sakiadis, B. C. 1961*b* Boundary-layer behaviour on continuous solid surfaces. II. The boundary layer on a continuous flat surface. *AIChe J.* **7** (2), 221–225.

Sander, W. & Weigand, B. 2008 Direct numerical simulation and analysis of instability enhancing parameters in liquid sheets at moderate Reynolds numbers. *Phys. Fluids* **20**, 053301.

Schmid, P. J. & Henningson, D. S. 2001 *Stability and Transition in Shear Flows*. Springer.

Söderberg, L. D. 2003 Absolute and convective instability of a relaxational plane liquid jet. *J. Fluid Mech.* **493**, 89–119.

Söderberg, L. D. & Alfredsson, P. H. 1998 Experimental and theoretical stability investigations of plane liquid jets. *Eur. J. Mech.* B/*Fluids* **17** (5), 689–737.

Squire, H. B. 1953 Investigation of the instability of a moving liquid film. *Br. J. Appl. Phys.* **4**, 167–169.

Teng, C. H., Lin, S. P. & Chen, J. N. 1997 Absolute and convective instability of a viscous liquid curtain in a viscous gas. *J. Fluid Mech.* **332**, 105–120.

Weber, C. 1931 Zum Zerfall eines Flüssigkeitsstrahles. *Z. Angew. Math. Mech.* **11**, 136–154.